In situ Raman analysis of reduced-graphene oxide-based electroactive nanofluids

Monica Parpal [a], Alexandros El Sachat [b], Clivia M. Sotomayor Torres [c,d], Pedro Gómez-Romero [c], Daniel Rueda-García [c,*], Emigdio Chavez-Angel [c,*]

[a] *Departament de Química, Universitat Autònoma de Barcelona, Cerdanyola del Vallès, 08193 Barcelona, Spain*
[b] *Institute of Nanoscience and Nanotechnology, National Center for Scientific Research "Demokritos", 15341 Agia Paraskevi, Athens, Greece*
[c] *Catalan Institute of Nanoscience and Nanotechnology, CSIC and The Barcelona Institute of Science and Technology (BIST), Campus UAB, Bellaterra, 08193 Barcelona, Spain*
[d] *ICREA, Passeig Lluis Companys 23, 08010 Barcelona, Spain*

ARTICLE INFO

ABSTRACT

This study investigates the effect of an applied stationary voltage on the vibrational properties of 1 M H_2SO_4 and H_2SO_4-based reduced-graphene oxide (rGO) nanofluids, commonly used as electrolytes in electrochemical cells. Our findings indicate that the energy of the symmetric stretching vibrations of H_2SO_4 remains unaffected by the electric field. However, a slight deviation toward lower energy and an enhancement of Raman intensity are observed in the asymmetric stretching vibration of H_2SO_4 due to the applied voltage. Furthermore, the addition of rGO to the base fluid produces a significant redshift in the symmetric stretching bands, indicating that the presence of rGO produces important changes at the macroscopic level in the base fluid. Synchronous and asynchronous maps further uncover the positive correlations between the D and G bands as well as between rGO and the base fluid bands. Specifically, the asynchronous map revealed complex dynamics between the rGO and H_2SO_4 bands and only positive correlations between H_2SO_4 bands. These results demonstrate the potential of Raman spectroscopy as a non-invasive technique to systematically study the influence of electric fields on the vibrational properties of fluids and nanofluids, which can ultimately lead to the development of significantly more efficient electrochemical cells.

1. Introduction

Graphene-based nanofluids (G-based NFs) have garnered significant attention in the research community because of their remarkable heat transfer capabilities [1–5]. Notably, the dispersion of small amounts of graphene within NFs has showed a pronounced impact on the thermal conductivity. Similarly, electroactive graphene NFs exhibit enhanced charge transfer behaviour with non-linear respone [6–9], thus can be effectively used as liquid electrodes or electrolytes.This emerging evidence is particularly intriguing, because it highlights the potential of graphene particles to significantly modify various material properties beyond thermal and electrical conductivity. This includes the potential modification of the intermolecular potential of the base fluid [10] and the formation of solid-like surfaces around the graphene flakes [2,11], which strongly affects rheological [12,13] and acoustic properties [2]. Surprisingly, the degree of dilution of the particles in these NFs is such that, in principle, no direct interactions between the particles are expected.

Recently, the use of graphene and its derivatives, such as reduced graphene oxide (r-GO), as solid electrode materials for energy storage in supercapacitors and batteries has gained significant attention. [14–16]. Nonetheless, G-based NFs as flowing liquid electrodes show great potential for the advancement of energy storage flow cells. This novel approach allows great flexibility in the design and engineering of flow cells, which leads to enhanced energy storage capabilities and improved performance [6,8,17–19].

The incorporation of rGO nanoparticles (NPs) into aqueous sulfuric acid results in first, the creation of a capacitive energy-storing NFs [6], and second, the establishment of an effective conductive substrate for nanoparticles, like $LiFePO_4$ (LFP), commonly employed in battery applications [18].

In previous studies, we have demonstrated the potential use of a

---

* Corresponding authors.
E-mail addresses: drueda@mobbio.com (D. Rueda-García), emigdio.chavez@icn2.cat (E. Chavez-Angel).

dispersion of 0.025 wt% rGO in 1 M H2SO4 aqueous electrolyte as a supercapacitive nanofluid in a flow cell. Our work revealed remarkably high capacitive energy storage capabilities, comparable to the solid counterparts (normalized per unit mass of active material), but operating at faster rates [6]. Notably, similar conclusions were drawn in hybrid rGO-polyoxometalates (POM) NFs, which exhibited even higher energy densities [17]. These findings strongly indicate that the presence of dispersed rGO sheets within the NFs facilitates efficient charge transfer from the current collector to the POM, despite their low concentration.

Moreover, we explored the exceptional charge transfer properties of rGO dispersions by conducting a comprehensive investigation of a nanofluid, incorporating both rGO and LFP NPs. Notably, the resulted material was not considered as hybrid material, as the rGO and LFP particles were not bonded but rather mixed together into the nanofluid. These findings revealed that a NF containing only LFP NPs did not show any electrochemical response. In contrast a NF that contains both LFP and rGO enabled full charge/discharge of LFP NPs, exhibiting even better performance (normalized per mass of active material) than a solid electrode with bare LFP NPs (i.e., uncoated with carbon). In particular, the specific capacitance of uncoated LFP NPs dispersed in rGO-based NFs was observed to be commensurate with that of LFP nanoparticles coated with rGO or other carbon materials in a solid electrode configuration. These results provide new insights regarding the excellent charge transfer capabilities of rGO dispersions.

Furthermore, we studied the thermal properties of G-based NFs dispersed in dimethylformamide (DMF) and dimethylacetamide (DMAC). We found a significant increase in the thermal conductivity in DMF, by almost a factor of 2, using only a 0.18 wt% concentration of graphene [2]. Interestingly, this enhancement was accompanied by a shift and broadening of specific Raman modes of DMF, which were found to be proportional to the concentration of the dispersed graphene. Similar modifications reported in DMAC NFs [20]. These results suggest that graphene has a great influence on all DMF and DMAC molecules, despite the highly diluted nature of the NFs.

In this work, we introduce a novel experimental setup and methodology designed for the investigation of the impact of an external electric field on rGO-based NFs dispersed in 1 M H_2SO_4 through Raman spectroscopy. These fluids are widely used electrolytes in electrochemical cells. The Raman spectral analysis demonstrated that even at a low concentration, the rGO signal underwent proportional modification in response to the applied potential between the electrodes, despite its low concentration. Furthermore, we observed that the presence of rGO modified the Raman signal of the base fluid, as reflected in the shift of some Raman modes of H_2SO_4. These findings provides evidence of the influence of dilute rGO sheets on the bulk properties of host fluid. Our observations have significant implications for the optimization of electrochemical cells, particularly for the development of more efficient electrolytes. The use of Raman spectroscopy as a non-invasive technique allowed the comprehensive exploration of the vibrational modes of the fluids, yielding insightful information on their behaviour under the influence of external electric fields.

For the analysis of the weak Raman features within the rGO NFs and the base fluid, a two-dimensional correlation spectroscopy (2DCOS) technique was employed. The 2DCOS is a model-free spectroscopic tool that correlates perturbation-induced spectral intensity changes with the spectroscopic response of the system. This method is ideal to reveal intricate or subtle spectral variations observed when a system is exposed to an external perturbation, which may be challenging to discern using only visual inspection. The identification of these changes can be detected by examining the correlation peaks appearing at a given frequency on the 2D spectral plane. The 2DCOS analyses involve two types of contour maps: synchronous and asynchronous correlations.

The synchronous contour map (denoted as $\Phi(w_1, w_2)$) represents simultaneous or coincidental spectral variations at two different frequencies, w_1 and w_2, during the observation interval with respect to the

external perturbation. Correlation peaks appear at both diagonal and off-diagonal positions. Peaks positioned on the diagonal correspond mathematically to the autocorrelation function, akin to the continuous form of statistical variance, and are called auto-peaks. Auto-peaks always exhibit positive signs, representing the extent to which the spectral signal can alter its intensity in response to an external perturbation applied to the system. Off-diagonal peaks (or cross peaks) represent simultaneous or coincidental variations in two distinct intensity signals observed at coordinates w_1 and w_2. This synchronicity implies a potential interconnected or correlated source for the signal fluctuations. The sign of cross-peaks can be either positive or negative. A positive correlation indicates that the perturbation affects both peaks simultaneously, causing their intensities to either increase or decrease in response to external stimuli. On the contrary, a negative correlation indicates that one of the signals is increasing while the other is decreasing with respect to the perturbation.

On the other hand, the asynchronous map (denoted as $\Psi(w_1, w_2)$) represents the non-simultaneous or sequential variations in spectral intensities with respect to the perturbation. This type of contour plot lacks a diagonal peak and is characterized solely by cross peaks. The emergence of an asynchronous cross peak will appear when the intensity of two measured signals (w_1 and w_2) suffer out-of-phase variations, characterized by either delayed or accelerated changes with respect to each other. Moreover, the combination of these contour plots offers a distinctive capability to infer the sequence of spectral intensity changes based on the sign of cross peaks. When $\Phi(w_1, w_2)$ and $\Psi(w_1, w_2)$ have the same sign, it implies that the spectral intensity variation at w_1 predominantly precedes that at w_2. Conversely, if the signs differ, the order is reversed. In cases where $\Psi(w_1, w_2) = 0$ and $\Phi(w_1, w_2) \neq 0$, the spectral intensities at the two wave numbers, w_1 and w_2, exhibit complete synchronization. It is important to note that 2DCOS maps only give the order of spectral intensity variations but not the order of the presence of particular species contributing to the spectral signals. [21,22].

2. Methodology

Reduce graphene oxide has been synthesized via a modified Hummer's method [2,6,23] from graphite (Sigma-Aldrich, purity >99 % and size <20 um, St. Louis, MO, USA). Specifically, 5 g of NaNO3 and 225 ml of H2SO4 were added to 5 g of graphite, and the mixture was stirred for 30 min while in an ice bath. The use of a combination of NaNO3 and H2SO4 creates a highly oxidizing environment that leads to the exfoliation of graphite. Subsequently, 25 g of KMnO4 were added to the solution to provide additional oxidizing agents and to enhance the exfoliation process, and the resulting solution was stirred at 50 °C for two hours. Afterward, 500 ml of deionized water and 30 ml of H2O2 (35 %) were slowly added to the solution to remove any remaining metallic impurity. The solution was then washed with dilute HCl, and the GO product was washed again with 500 ml of concentrated HCl (37 %) to remove any remaining organic impurity. rGO was prepared by subjecting the GO sample to high-temperature treatment at 800 °C in a nitrogen atmosphere for one hour. This process helps to remove the oxygen-containing functional groups present in GO and restores the sp2 hybridization of the carbon atoms. Once the rGO was synthesized, three nanofluid formulations were prepared for this study using H2SO4 1 M as base fluid. The NFs were prepared by dispersing 0.025 % wt of rGO in the base fluid using a sonicator (Ovan) for 30 min at 40 Hz. In two of these samples triton X-100 (TRX) was added as surfactant in two concentrations (0.5 and 1.0 % TRX). Then, in total four samples were analysed and labelled as follows: base fluid (rGO-free), 0.0 % TRX, 0.5 % TRX and 1.0 % TRX. The last three corresponding to the rGO-based NFs.

The Raman spectra were recorded using a T64000 Raman spectrometer manufactured by HORIBA Jobin Yvon. The fluids were placed into a custom-built electrochemical cell comprising of two platinum electrodes, where one electrode functioned as the working electrode, while the other served as the counter and reference electrode (see Fig. S1
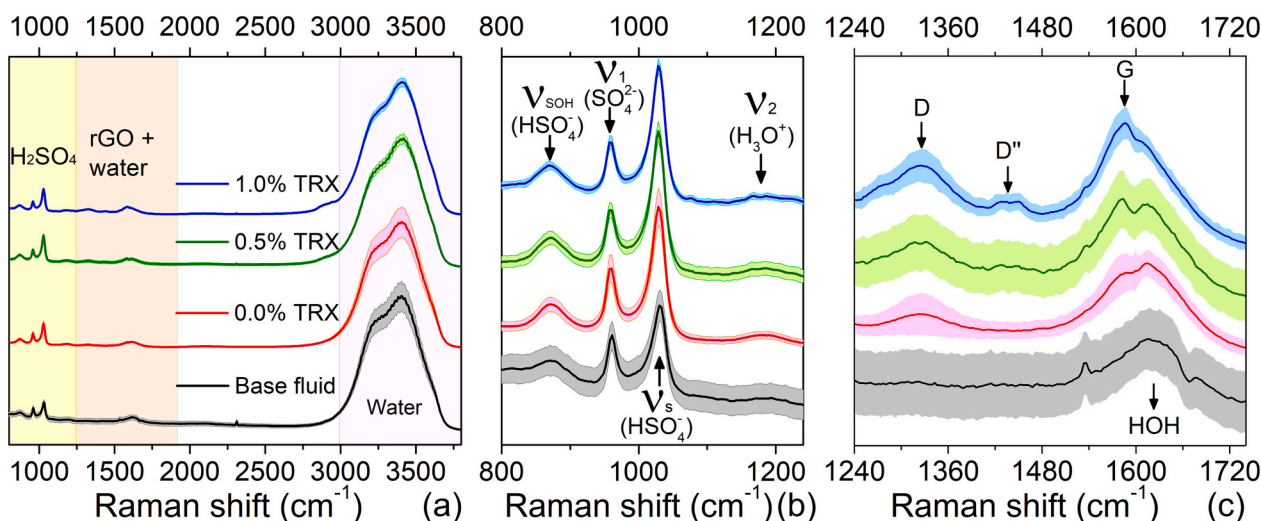
Fig. 1. Average (solid lines) and standard deviation (shaded areas) of the raw Raman spectra of four samples under voltage excitation: (a) the full spectra, (b) magnification from 800 to 1200 cm^{-1} and (c) magnification from 1240 to 1720 cm^{-1}. The black spectrum corresponds to the 1 M H_2SO_4 base fluid without rGO, while all other spectra have a 0.025 % weight concentration of rGO with different concentration of surfactant. %TRX values refer to the concentration of triton X-100 surfactant. The highlighted areas in (a) indicate the zones in which Raman modes of the H_2SO_4 (yellow), rGO and water (orange) and pure water (violet) can be observed.

in supporting information). The two-electrode cell was linked to a potentiometer (Biologic SP200) capable of regulating voltages ranging from 0 to 1 V in increments of 0.1 V. Subsequently, a green diode laser (λ = 532 nm) was focused between the electrodes utilizing a 50× long working distance microscope objective. The laser power was maintained at minimal levels (<1 mW) to avoid potential self-heating effects. To ensure consistency, the spectra of the fluids were recorded 20 times at different positions within the cell, in proximity to the electrodes while maintaining the same focal plane and applied voltage. The fitting of whole set of data was done with the open source software package Orange, Bioinformatics Laboratory of the University of Ljubljana, version 3.31, and the spectroscopy add-on, version 0.6.3 [24–26]. Within Orange, all spectra were baseline corrected (rubber band) and normalized by the area of strongest Raman peak of water (2790–3800 cm^{-1}). Then, treated spectra were fitted to Lorentzian functions. The analysis of the two-dimensional correlation spectroscopy was performed with Mat2d-corr Matlab toolbox [27]. To calculate the 2DCOS map we used the average spectra for each voltage (20 spectra per voltage step) and using applied voltage as the external perturbation. Prior to the averaging, the whole dataset was baselined and normalized using the same procedure described above. The whole average spectrum was used as a reference following the same procedure described previously [28].

3. Raman results

Fig. 1 shows the raw Raman spectra of the four nanofluids analysed in this work. The average spectrum of each fluid is represented by solid lines, while the shaded areas around each average correspond to the standard deviation. Both the averaged spectra and the standard deviation were calculated over the entire experiment, which involved an average of 20 spectra per voltage and a total of 220 spectra per experiment. The strongest broad band around 3400 cm^{-1} corresponds to OH stretching vibration of water [29]. The three peaks shown in Fig. 1b are associated to H_2SO_4. These peaks correspond to the asymmetric stretching vibration of HSO_4^- (ν_{SOH}, ~ 870 cm^{-1}), the total symmetric stretching vibration of SO_4^{2-} (ν_1, ~ 960 cm^{-1}) and the symmetric stretching vibration of HSO_4^- ions (ν_S, ~ 1030 cm^{-1}). A weak band around 1200 cm^{-1} is also associated with H_2SO_4 and is attributed to a bending mode of H_3O^+ ions (ν_2), which is strongly coupled with HSO_4^- and SO_4^{2-} ions [30]. Additionally, the presence of bands of rGO is
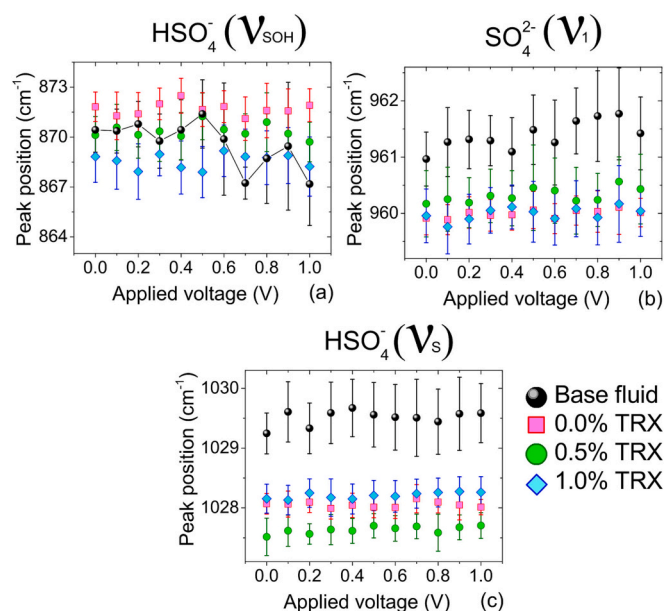

Fig. 2. Peak position of three Raman modes of H_2SO_4 shown in Fig. 1b: (a) asymmetric stretching vibration of HSO_4^- (ν_{SOH}), (b) symmetric stretching vibration of SO_4^{2-} (ν_1) and (c) symmetric stretching vibration of HSO_4^- ions (ν_S).

observed in Fig. 1c around 1320 cm^{-1} (D), 1440 cm^{-1} (D″) and 1600 cm^{-1} (G) [31,32], with the latter convoluted with the HOH bending band of water [29]. It is interesting to note a slight increase in the D and G peaks as the amount of TRX increases. The higher percentage of TRX contributes to a more effective dispersion of the nanoparticles, consequently enhancing the likelihood of optimal illumination by the Raman laser during the experiment. Conversely, the absence of TRX may result in particle agglomeration and precipitation, leading to reduced laser illumination and a subsequent decrease in Raman intensity.

In Fig. 2, we present the peak positions of the main Raman bands of H_2SO_4 as a function of the applied voltage for four different electrolytes. The peak positions (dots) represent the mean of each fitted band across all voltages, with the error bars indicating the standard deviation. Our
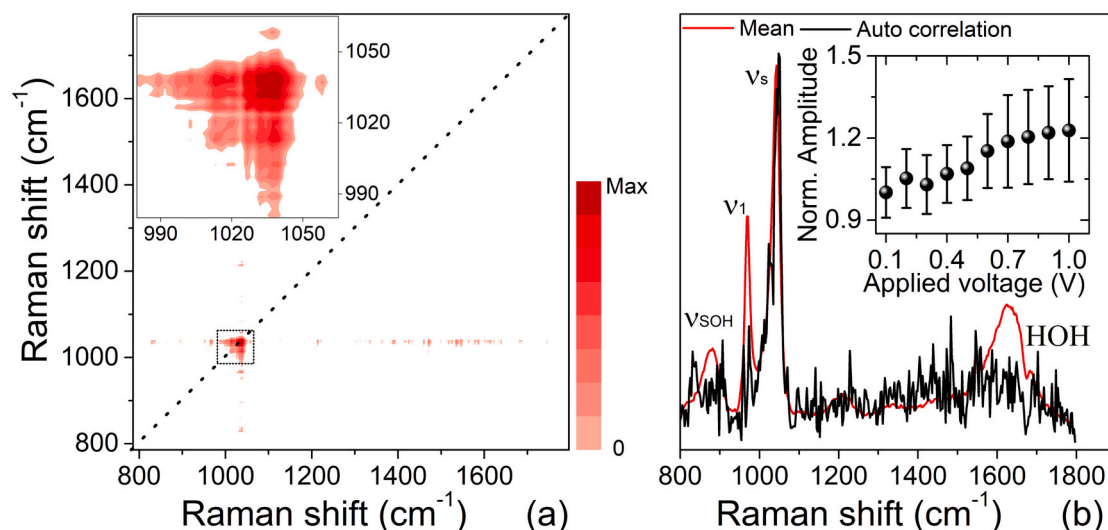
Fig. 3. (a) Synchronous two-dimensional correlation map of H_2SO_4 base fluid. The dashed line indicates the auto correlation spectrum. (Inset) zoom around the main auto peak. (b) Auto correlation (black line) and mean spectra (red line) of based fluid. (Inset) Normalized fitted amplitude of ν_s mode as function of applied voltage.

analysis indicates that there is no significant effect on the band position of the ν_1 and ν_s modes as the voltage increases. However, a small deviation toward lower energy can be observed in the ν_{SOH} peak of the base fluid (black dots in Fig. 2a and Fig. S2). This monotonous shifting of the peak position is also visible in the shape of the synchronous 2DCOS map (inset Fig. 3a), which exhibits the characteristic butterfly shape, indicative of a monotonous displacement of the band position with respect to the applied perturbation [21,33].

Furthermore, a substantial redshift of the ν_1 (~960 cm^{-1}) and ν_s (~1030 cm^{-1}) bands is evident as rGO is added to the solution. Similar shifts were previously shown in graphene-based nanofluids dispersed in DMAC and DMF [2,20]. We observed a monotonous blue shift in specific Raman modes of DMF- and DMAC-graphene NF as the content of graphene increased. This effect indicates that there is a strong modification of the interatomic potential of the fluids as a function of graphene concentration. Such displacement could also suggest a similar effect on the H_2SO_4 base fluid.

A single auto peak around 1030 cm^{-1} band is observed in synchronous 2DCOS map (Fig. 3a) and in the auto correlation spectrum (Fig. 3b) H_2SO_4 base fluid. This indicates that the applied voltage (i.e., the external perturbation) induces a significant modification on the amplitude of the ν_s band in the base fluid. The rest of the Raman modes did not exhibit a significant variation in signal, indicating that the rest of the peaks are not influenced by the external field. A monotonous increase of the fitted ν_s band is also shown in the inset of Fig. 3b indicating an enhancement of the signal induced by the applied voltage. Andrews and Blake proposed two mechanisms for enhancing the Raman signal of a pure fluid under a stationary electric field [34]. The first mechanism involves the electro-optical interaction between the external field and the molecules of the fluid. This interaction can perturb molecular wave functions, resulting in the modfication of the Raman selection rules, the activation of forbidden modes, or a shift in band frequency. The second mechanism is associated with the alignment of molecules with a permanent dipole moment in the direction of the electric field. In this case, the anisotropic distribution of molecular orientations within the fluid results in changes in the intensity of Raman modes. It is worth noting that the first mechanism is commonly referred to as the Stark effect [35,36], while the second one also modifies the viscosity of the fluids and is known as the electrorheological effect [37]. Both the Stark and the electrorheology effects can potentially modify the Raman signal intensity in a fluid, as they both involve changes in the polarizability and/or dipole moment of the molecules due to the applied field. The Stark effect tends to shift the energy levels of the molecules and thus
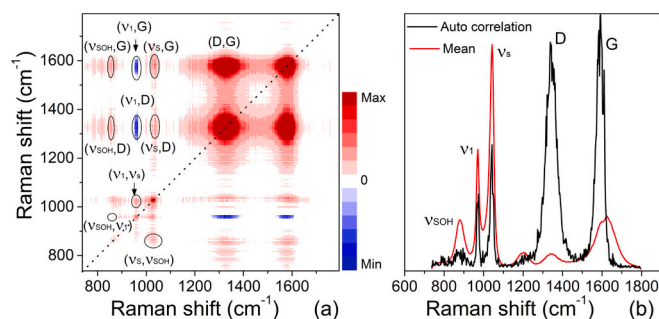
modify the frequencies of the Raman scattering, while the electro-rheology effect can induce changes in the orientation and alignment of the molecules and thus modify their Raman cross-sections. However, the magnitude and direction of these effects can depend on the properties of the fluid and the electric field, and they can potentially interfere with each other in complex ways. Therefore, a detailed experimental and theoretical analysis is required to determine which effect is predominant in a given system. The polar nature of H_2SO_4 and the observed shift in the band position indicate that the Stark effect is likely the primary mechanism responsible for the amplified Raman peak and the displacement of the mode. Nonetheless, the addition of rGO to the system results in the stabilization of the ν_{SHO} band, and its position remains nearly constant under the influence of the external field. The electrically insulating and polarizable properties of rGO [38] enable the alignment of rGO nanomaterial with the external field, potentially suppressing the effect of the Stark effect on H_2SO_4. Nevertheless, further research is necessary to gain a more comprehensive understanding of both phenomena.

Fig. 4 displays the synchronous 2DCOS map, auto-correlation, and averaged spectra of the 0.0 % TRX sample. A larger number of auto- and cross-peaks are observed, indicating the presence of spectral intensity changes induced in the nanofluid by the external field. Notably, the auto-correlation spectrum (Fig. 4b) shows a complete deconvolution of the G mode (~1600 cm-1) with respect to the HOH mode of water, suggesting that the subtle changes arise from the rGO peak rather than the HOH band. Moreover, the G and D bands display a positive
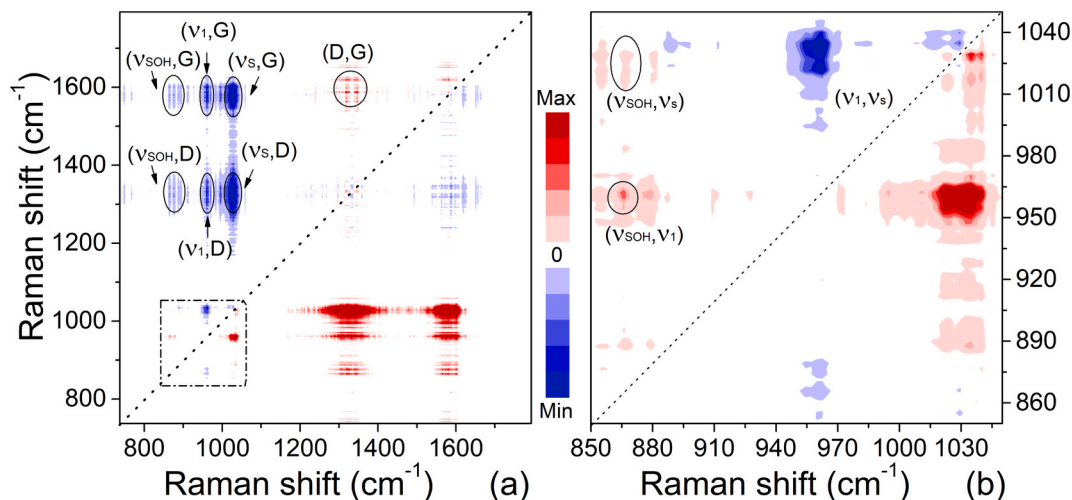

Fig. 4. (a) Synchronous two-dimensional correlation map and (b) autocorrelation (black line) and mean (red line) spectra of 0.0 % TRX 1 M H_2SO_4 rGO-based nanofluid.

Fig. 5. Asynchronous two-dimensional correlation map of 0.0 TRX base fluid. (a) Full spectra window (b) Magnification of black square marked in (a).
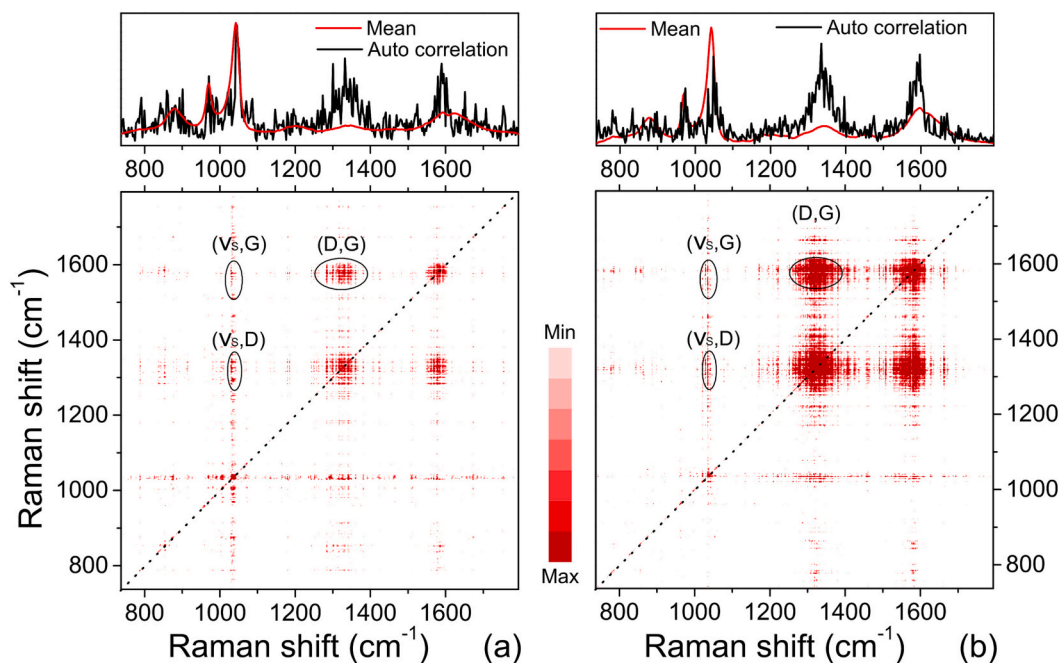

Fig. 6. Synchronous two-dimensional correlation map of: (a) 0.5 % TRX and (b) 1.0 % TRX sample.

correlation, indicating that their intensities respond similarly to the perturbation. The synchronous and asynchronous maps (Fig. 5a) shows a positive sign at the spectra coordinates (D, G), indicating that the intensity changes of the D band occur before those of the G band. Additionally, the synchronous map shows that the rGO bands are also correlated with the bands of the base fluid. Positive synchronous correlations are observed at the spectral coordinates (ν_{SOH}, D), (ν_{SOH}, G), (ν_S, D), and (ν_S, G), while negative correlations are observed at (ν_1, D) and (ν_1, G). On the other hand, the asynchronous map reveals a negative correlation between all rGO and H_2SO_4 mode pairs. This suggests that the intensity variation observed in ν_1 occurs prior than D and G since $\Phi(\nu 1, G)$ and $\Phi(\nu 1, D)$ share the same sign as $\Psi(\nu 1, G)$ and $\Psi(\nu 1, D)$, respectively. Conversely, the intensity alterations in ν_S and ν_{SOH} occur after those in D and G, as indicated by the synchronous and asynchronous maps exhibiting different signs.

Regarding the H_2SO_4 modes, a careful analysis of the synchronous and asynchronous maps reveals several correlations between the different mode-pairs. Specifically, in the synchronous map, we can

observe that all mode-pairs, including ν_S, ν_1, and ν_{SOH}, exhibit a positive correlations. However, upon zooming in on the asynchronous map around the H_2SO_4 peaks (Fig. 5b), we can see positive correlations of (ν_{SOH}, ν_1) and (ν_{SOH}, ν_S) and negative correlation of (ν_1, ν_S). These findings suggest that the ν_{SOH} mode occurs prior both the ν_1 and ν_S modes, while the ν_1 mode occurs after the ν_S mode. In the case of the remaining samples with 0.5 % and 1.0 % TRX, the 2DCOS synchronous map and the auto correlation spectra (Fig. 6a and b) indicate the detection of very weak features of correlation. In both fluids, positive correlation is observed between (D, G), (ν_S, D), and (ν_S, G), which confirms the observations made in the 0.0 % TRX sample. However, in terms of the asynchronous map, the features were too feeble to provide any meaningful information about all the pairs. Therefore, it is clear that the presence of TRX surfactant in the nanofluid plays a significant role in the detection of the correlation between the Raman bands, as the absence of TRX in the 0.0 % sample resulted in the strongest correlation features.

4. Conclusions

In conclusion, we have investigated the effect of an external electric field on the Raman spectra of H_2SO_4-based nanofluids with rGO. The results revealed a significant modification in the amplitude of the band induced by the applied voltage, suggesting an enhancement of the Raman peak. We also observed a weak voltage-dependence of ν_{SOH} mode of the base fluid, which disappears to add rGO to the solution. Moreover, a large redshift of the ν_1 and ν_s bands was found due to the addition of rGO. These two bands showed a rather constant value of their position as the voltage was varied in all the fluids. The synchronous and asynchronous maps reveal several correlations between the different mode-pairs of H_2SO_4. The findings suggest that the changes of ν_{SOH} mode occurs prior both the ν_1 and ν_S modes, while the changes of ν_1 mode occurs after the ν_S mode. Notably, the introduction of rGO into the H_2SO_4 base fluid facilitated the detection of the correlation between the three primary Raman modes of H_2SO_4 in absence of the surfactant. Conversely, the addition of the surfactant appeared to conceal such correlation, thereby suggesting that triton X-100 acts as a passivating agent on the rGO surface and masks intermolecular interactions. These findings shed light on the role of surfactants in modulating the Raman signals of graphene-based materials, which could be significant for the development of efficient graphene-based sensors and devices. Moreover, our findings provide valuable insights into the behaviour of H_2SO_4-based nanofluids with rGO under an external electric field, which can be useful for various technological applications.

CRediT authorship contribution statement

Conceptualization, P.G.-R., C.M.S.T., D.R.-G. and E.C.-A.; Methodology, D.R.-G. and E.C.-A.; Validation, P.G.-R. and C.M.S.T.; Formal analysis, M.P. and E.C.A.; Investigation, M.P., D.R.-G. and E.C.-A.; Resources, C.M.S.T. and P.G.-R.; Data curation, A.E.S. and E.C.A.; Writing—original draft, A.E.S., D.R.-G. and E.C.-A.; Writing—review & editing, All; Supervision, C.M.S.T. and P.G.-R.; Funding acquisition, C.M.S.T. and P.G.-R. All authors have read and agreed to the published version of the manuscript.

Declaration of competing interest

The authors declare the following financial interests/personal relationships which may be considered as potential competing interests: Pedro Gomez- Romero reports financial support was provided by Spanish Scientific Research Council. Alexandros El Sachat reports financial support was provided by EU-H2020 research. Clivia Sotomayor Torres reports financial support was provided by European Research Council. Emigdio Chavez Angel reports financial support was provided by European Research Council.

Data availability

Data will be made available on request.

Acknowledgements

Appendix A. Supplementary data

Supplementary data to this article can be found online at https://doi.org/10.1016/j.diamond.2023.110541.

References

[1] E. Sadeghinezhad, M. Mehrali, R. Saidur, M. Mehrali, S. Tahan Latibari, A.R. Akhiani, H.S.C. Metselaar, A comprehensive review on graphene nanofluids: recent research, development and applications, Energ. Conver. Manage. 111 (2016) 466–487, https://doi.org/10.1016/j.enconman.2016.01.004.

[2] M.R. Rodríguez-Laguna, A. Castro-Alvarez, M. Sledzinska, J. Maire, F. Costanzo, B. Ensing, M. Pruneda, P. Ordejón, C.M. Sotomayor Torres, P. Gómez-Romero, E. Chávez-Ángel, Mechanisms behind the enhancement of thermal properties of graphene nanofluids, Nanoscale 10 (2018) 15402–15409, https://doi.org/10.1039/C8NR02762E.

[3] D.P. Barai, B.A. Bhanvase, S.H. Sonawane, A review on graphene derivatives-based nanofluids: investigation on properties and heat transfer characteristics, Ind. Eng. Chem. Res. 59 (2020) 10231–10277, https://doi.org/10.1021/acs.iecr.0c00865.

[4] B. Mehta, D. Subhedar, Review on mechanism and parameters affecting thermal conductivity of nanofluid, Mater. Today Proc. 56 (2022) 2031–2037, https://doi.org/10.1016/j.matpr.2021.11.374.

[5] H. Lin, Q. Jian, X. Bai, D. Li, Z. Huang, W. Huang, S. Feng, Z. Cheng, Recent advances in thermal conductivity and thermal applications of graphene and its derivatives nanofluids, Appl. Therm. Eng. 218 (2023), 119176, https://doi.org/10.1016/j.applthermaleng.2022.119176.

[6] D.P. Dubal, P. Gomez-Romero, Electroactive graphene nanofluids for fast energy storage, 2D Mater. 3 (2016) 31004, https://doi.org/10.1088/2053-1583/3/3/031004.

[7] J. Lobato, E. Mena, M. Millán, Improving a redox flow battery working under realistic conditions by using of graphene based nanofluids, ChemistrySelect 2 (2017) 8446–8450, https://doi.org/10.1002/slct.201701042.

[8] S. Aberoumand, D. Dubal, P. Woodfield, K. Mahale, H.D. Pham, C. Padwal, T. Tung, M.J. Shiddiky, D.V. Dao, Reduced graphene oxide nanofluidic electrolyte with improved electrochemical properties for vanadium flow batteries, J. Energy Storage. 49 (2022), 104133, https://doi.org/10.1016/j.est.2022.104133.

[9] J. Kim, H. Park, Impact of nanofluidic electrolyte on the energy storage capacity in vanadium redox flow battery, Energy 160 (2018) 192–199, https://doi.org/10.1016/j.energy.2018.06.221.

[10] S. Sarkar, R.P. Selvam, Molecular dynamics simulation of effective thermal conductivity and study of enhanced thermal transport mechanism in nanofluids, J. Appl. Phys. 102 (2007), https://doi.org/10.1063/1.2785009.

[11] P. Keblinski, S.R. Phillpot, S.U.S. Choi, J.A. Eastman, Mechanisms of heat flow in suspensions of nano-sized particles (nanofluids), Int. J. Heat Mass Transf. 45 (2002) 855–863, https://doi.org/10.1016/S0017-9310(01)00175-2.

[12] S. Hamze, D. Cabaleiro, P. Estellé, Graphene-based nanofluids: a comprehensive review about rheological behavior and dynamic viscosity, J. Mol. Liq. 325 (2021), 115207, https://doi.org/10.1016/j.molliq.2020.115207.

[13] A. Ahmadi Nadooshan, H. Eshgarf, M. Afrand, Evaluating the effects of different parameters on rheological behavior of nanofluids: a comprehensive review, Powder Technol. 338 (2018) 342–353, https://doi.org/10.1016/j.powtec.2018.07.018.

[14] M. Pumera, Electrochemistry of graphene: new horizons for sensing and energy storage, Chem. Rec. 9 (2009) 211–223, https://doi.org/10.1002/tcr.200900008.

[15] D. Yang, C. Bock, Laser reduced graphene for supercapacitor applications, J. Power Sources 337 (2017) 73–81, https://doi.org/10.1016/j.jpowsour.2016.10.108.

[16] E.E. Miller, Y. Hua, F.H. Tezel, Materials for energy storage: review of electrode materials and methods of increasing capacitance for supercapacitors, J. Energy Storage 20 (2018) 30–40, https://doi.org/10.1016/j.est.2018.08.009.

[17] D.P. Dubal, D. Rueda-Garcia, C. Marchante, R. Benages, P. Gomez-Romero, Hybrid graphene-polyoxometalates nanofluids as liquid electrodes for dual energy storage in novel flow cells, Chem. Rec. 18 (2018) 1076–1084, https://doi.org/10.1002/tcr.201700116.

[18] D. Rueda-Garcia, Z. Cabán-Huertas, S. Sánchez-Ribot, C. Marchante, R. Benages, D.P. Dubal, O. Ayyad, P. Gómez-Romero, Battery and supercapacitor materials in flow cells. Electrochemical energy storage in a LiFePO4/reduced graphene oxide aqueous nanofluid, Electrochim. Acta 281 (2018) 594–600, https://doi.org/10.1016/j.electacta.2018.05.151.

[19] M.S. Alfonso, H. Parant, J. Yuan, W. Neri, E. Laurichesse, K. Kampioti, A. Colin, P. Poulin, Highly conductive colloidal carbon based suspension for flow-assisted electrochemical systems, IScience 24 (2021), 102456, https://doi.org/10.1016/j.isci.2021.102456.

[20] M. del R. Rodríguez-Laguna, P. Gómez-Romero, C.M. Sotomayor Torres, E. Chavez-Angel, Modification of the Raman spectra in graphene-based nanofluids and its correlation with thermal properties, Nanomaterials 9 (2019) 804, https://doi.org/10.3390/nano9050804.

[21] I. Noda, Y. Ozaki, Generalized two-dimensional correlation spectroscopy in practice, in: Two-Dimensional Correl. Spectrosc. - Appl. Vib. Opt. Spectrosc, John Wiley & Sons, Ltd, Chichester, UK, 2005, pp. 47–64, https://doi.org/10.1002/0470012404.ch4.

[22] I. Noda, Advances in Two-Dimensional Correlation Spectroscopy (2DCOS), in: Front. Adv. Mol. Spectrosc., Elsevier, 2018, pp. 47–75, https://doi.org/10.1016/B978-0-12-811220-5.00002-2.

[23] W.S. Hummers, R.E. Offeman, Preparation of graphitic oxide, J. Am. Chem. Soc. 80 (1958) 1339, https://doi.org/10.1021/ja01539a017.

[24] M. Toplak, S.T. Read, C. Sandt, F. Borondics, L. Vaccari, H.J. Byrne, T.P. Wrobel, Quasar: Easy Machine Learning for Biospectroscopy, Cells 10 (2021) 2300, https://doi.org/10.3390/CELLS10092300.

[25] J. Demsar, T. Curk, A. Erjavec, C. Gorup, T. Hocevar, M. Milutinovic, M. Mozina, M. Polajnar, M. Toplak, A. Staric, M. Stajdohar, L. Umek, L. Zagar, J. Zbontar, M. Zitnik, B. Zupan, Orange: data mining toolbox in python, J. Mach. Learn. Res. 14 (2013) 2349–2353. http://jmlr.org/papers/v14/demsar13a.html.

[26] M. Toplak, G. Birarda, S. Read, C. Sandt, S.M. Rosendahl, L. Vaccari, J. Demšar, F. Borondics, Infrared orange: connecting hyperspectral data with machine learning, Synchrotron Radiat. News. 30 (2017) 40–45, https://doi.org/10.1080/08940886.2017.1338424.

[27] P. Lasch, I. Noda, Two-dimensional correlation spectroscopy (2D-COS) for analysis of spatially resolved vibrational spectra, Appl. Spectrosc. 73 (2019) 359–379, https://doi.org/10.1177/0003702818819880.

[28] E. Chavez-Angel, B. Puertas, M. Kreuzer, R. Soliva Fortuny, R.C. Ng, A. Castro-Alvarez, C.M. Sotomayor Torres, Spectroscopic and thermal characterization of extra virgin olive oil adulterated with edible oils, Foods 11 (2022) 1304, https://doi.org/10.3390/foods11091304.

[29] D.M. Carey, G.M. Korenowski, Measurement of the Raman spectrum of liquid water, J. Chem. Phys. 108 (1998) 2669–2675, https://doi.org/10.1063/1.475659.

[30] K. Tomikawa, H. Kanno, Raman study of sulfuric acid at low temperatures, J. Phys. Chem. A 102 (1998) 6082–6088, https://doi.org/10.1021/jp980904v.

[31] A.A.K. King, B.R. Davies, N. Noorbehesht, P. Newman, T.L. Church, A.T. Harris, J. M. Razal, A.I. Minett, A new Raman metric for the characterisation of graphene oxide and its derivatives, Sci. Rep. 6 (2016) 19491, https://doi.org/10.1038/srep19491.

[32] A. Pinilla-Sánchez, E. Chávez-Angel, S. Murcia-López, N.M. Carretero, S. M. Palardonio, P. Xiao, D. Rueda-García, C.M. Sotomayor Torres, P. Gómez-Romero, J. Martorell, C. Ros, Controlling the electrochemical hydrogen generation and storage in graphene oxide by in-situ Raman spectroscopy, Carbon N. Y. 200 (2022) 227–235, https://doi.org/10.1016/j.carbon.2022.08.055.

[33] M.A. Czarnecki, Interpretation of two-dimensional correlation spectra: science or art? Appl. Spectrosc. 52 (1998) 1583–1590, https://doi.org/10.1366/0003702981943086.

[34] D.L. Andrews, N.P. Blake, Electric-field-induced Raman spectroscopy, J. Chem. Phys. 88 (1988) 6039–6048, https://doi.org/10.1063/1.454496.

[35] S. Zhang, R. Shi, X. Ma, L. Lu, Y. He, X. Zhang, Y. Wang, Y. Deng, Intrinsic electric fields in ionic liquids determined by vibrational stark effect spectroscopy and molecular dynamics simulation, Chem. - A Eur. J. 18 (2012) 11904–11908, https://doi.org/10.1002/chem.201201257.

[36] A. Chattopadhyay, S.G. Boxer, Vibrational stark effect spectroscopy, J. Am. Chem. Soc. 117 (1995) 1449–1450, https://doi.org/10.1021/ja00109a038.

[37] H. Block, J.P. Kelly, Electro-rheology, J. Phys. D Appl. Phys. 21 (1988) 1661–1677, https://doi.org/10.1088/0022-3727/21/12/001.

[38] Y. Wang, J. Yuan, X. Zhao, J. Yin, Electrorheological fluids of GO/graphene-based nanoplates, Materials (Basel) 15 (2022) 311, https://doi.org/10.3390/ma15010311.